Remote Sensing of Induced Liquefaction: TLS and SfM for a Full-Scale Blast Test

(Article begins on next page)

14 January 2025

1 **Remote sensing of induced liquefaction: TLS and SfM for a full scale blast test**

2 Arianna Pesci[1], Giordano Teza[2], Fabiana Loddo[3], Kyle Rollins[4], Paul Andersen[5], Luca Minarelli[6],

3 Sara Amoroso[7]

4 [1] Researcher, Istituto Nazionale di Geofisica e Vulcanologia, Sezione di Bologna, Via Donato Creti, 12, 40128

5 Bologna, Italy (Corresponding author). http://orcid.org/0000-0003-1863-3132. Email: arianna.pesci@ingv.it

6 [2] Researcher, Department of Physics and Astronomy, University of Bologna, Viale Berti Pichat 6/2, 40127 Bologna,

7 Italy. http://orcid.org/0000-0002-6902-5033. Email: giordano.teza@gmail.com

8 [3] Technologist, Istituto Nazionale di Geofisica e Vulcanologia, Sezione di Bologna, Via Donato Creti, 12, 40128

9 Bologna, Italy. http://orcid.org/0000-0002-1153-1021. Email: fabiana.loddo@ingv.it

10 [4] Professor, Department of Civil and Environmental Engineering, Brigham Young University, 430 Engineering

11 Building, Provo, UT 84602, USA. http://orcid.org/0000-0002-8977-6619. Email: rollinsk@byu.edu

12 [5] Research Assistant, Department of Civil and Environmental Engineering, Brigham Young University, 430

13 Engineering Building, Provo, UT 84602, USA. http://orcid.org/0000-0002-9084-4084. Email: paul.andersen@byu.edu

14 [6] Temporary Research Assistant, Istituto Nazionale di Geofisica e Vulcanologia, Sezione Roma1, Sede L'Aquila, Viale

15 Francesco Crispi 43, 67100 L'Aquila Italy. ORCID: 0000-0003-3602-9975. Email: luca.minarelli@ingv.it

16 [7] Assistant Professor, Department of Engineering and Geology, University of Chieti-Pescara, Viale Pindaro 42, 65129

17 Pescara, Italy; Research Associate, Istituto Nazionale di Geofisica e Vulcanologia, Sezione Roma 1, Sede L'Aquila,

18 Viale Francesco Crispi 43, 67100 L'Aquila, Italy. ORCID: 0000-0001-5835-079X. Email: sara.amoroso@unich.it

19

20 **Abstract**

21 Terrestrial Laser Scanning (TLS) and drone-based Structure from Motion photogrammetry (SfM)

22 allowed the study of soil deformations due to blast-induced liquefaction during an experiment

23 carried out on 4 June 2018. The research aimed at both evaluating the measurement quality and

24 estimating the Rammed Aggregate Piers (RAPs) effectiveness in mitigating the effects of soil

25 liquefaction. These effects mainly consist in subsidence and deposits of ejected and extruded

26 materials. The comparison between multi-temporal 3D models provided surface variation maps and

27 volume changes. In addition, classical topographical levelling allowed the measurement of sub-

28 surface vertical displacement along a specific cross-section. The results pointed out a significant

29 reduction, higher than 50%, of soil deformation in areas improved by RAPs installation; moreover,

30 the corresponding volume variations were no more than about 37% of those occurred in the not

31 improved area. Finally, a critical comparison between remote sensing and levelling suggested that

32 surface variation maps could underestimate the area lowering up to 15% in this kind of terrains.

33

34 **Author keywords**: Blast Test; Terrestrial Laser Scanning; Structure-from-Motion (SfM); Ground

35 deformation; Soil Liquefaction; Soil compaction.

36

37 **Introduction**

38 Soil liquefaction occurs in cases where a saturated soil temporarily loses strength and stiffness

39 caused by a sudden increase in excess porewater pressure due to, e.g., an earthquake or an

40 underground explosion. Liquefaction in saturated sandy deposits can induce severe damage to

41 structures during earthquakes. For this reason, Eurocode 8 (EN 2004), related to design of structures

42 for earthquake resistance, requires the quantitative evaluation of post-liquefaction settlements. The

43 studies on soil liquefaction are therefore important from both a scientific and an engineering

44 application point of view. However, these studies are difficult to implement for several reasons,

45 among which there are the stochastic nature of the earthquake loading, the uncertainties related to

46 geotechnical methods used to characterize the soil, the fact that often no data are available to allow

47 comparison between the pre-seismic and post-seismic conditions, and the need for reliable

48 numerical models (Győri et al. 2011). Blast tests, in which controlled blasting is carried out by

49 suitably positioned underground charges, are relatively recent, but they have already proved to be of

50 great importance (see e.g. Ashford et al. 2004; Saftner et al. 2015; Wentz et al. 2015; Amoroso et

51 al. 2017; 2020a).

52 Despite the potentially disastrous loss of soil strength and stiffness which can occur at the

53 time of the phenomenon that induces liquefaction, controlled blasting can also be beneficial as a

54 ground improvement technique for densification in clean sands (Finno et al. 2016). As porewater

55 pressures dissipate upwards following blasting, the sand reconsolidates to a denser more compact

56 state. The ground surface deformation plays an important role in compaction effect evaluation as

57 well as the estimate the subsoil changes that could be indirectly inferred (Pesci et al. 2018). In

58 general, mapping aimed at evaluating local subsidence is an important task to ensure building in

59 suitable areas. Examples are the recognition of sinkholes (Gutierrez et al. 2018) and analysis of

60 liquefaction susceptibility (Giona Bucci et al. 2018). Advanced statistical methods of data analysis

61 are also used for this purpose (Hu and Lui 2019). Dealing with remote sensing suitable technics for

62 monitoring surface variations, Terrestrial Laser Scanning (TLS), Structure-from-Motion

63 photogrammetry (SfM) and Ground-Based Interferometric Synthetic Aperture Radar (InSAR) are

64 highly efficient.

65   TLS provides point clouds, i.e. sets of XYZ coordinates of numerous points sampled on the

66 observed surface (Vosselman and Maas 2010). Currently available instruments can measure 10^4-10^6

67 points per second with 0.1-1 cm precision. Topographic mapping and spatial analyses can be

68 carried out directly on the point cloud or also on a digital model generated from the point cloud, in

69 particular a 2.5D model, which is the case of a Digital Terrain Model (DEM), or a 3D model like a

70 triangulated mesh. A discussion on experimental evaluation of the resolution of a TLS instrument is

71 in Pesci et al. (2011). Long range TLS instruments are powerful in geomorphological surveying

72 aimed at change detection (see e.g. Fey and Wichmann 2017).

73   SfM facilitates fast and inexpensive generation of accurate photorealistic point clouds and

74 digital models by means of sequences of images taken from a ground or an aerial platform

75 (generally an Unmanned Aerial System, UAS), or a combination of them. Good results in terms of

76 precision and resolution require data taken in favorable and consistent light conditions without

77 significant disturbances (like vegetation). For this reason, this technique is often used in geological

78 and geomorphological surveying (Brunier et al. 2016; Smith et al. 2016), also including harsh

79 environment (Rauhala et al. 2017). Tests on SfM precision and resolution show that deformation

80 patterns of at least 3-4 cm are detectable at 250 m distance, under the condition that the unstable

81   area is surrounded by stable areas. The resolution limit is about ~2.5 times the ground sampling

82   distance (GSD) (Pesci et al. 2020). This paper aims at evaluating the ground deformations induced

83   by a blast test in both natural and treated soils, from TLS and SfM surveys. Since in the test area

84   there where staff personnel engaged in several activities and various kinds of equipment,

85   instruments and objects, the survey scheduling was strongly constrained. Remote sensing activities

86   were carried out within relatively short time windows (Amoroso et al. 2020a).

87

88

89   **Test site**

90   The full-scale blast test took place on 4 June 2018 in the Bondeno area (Ferrara, Italy) in order to

91   study the effects of soil liquefaction and their possible mitigation by means of the installation of

92   Rammed Aggregate Piers (RAPs). Details about the RAP improvement technique are available in

93   Saftner et al. (2018). The geological setting of the area is characterized by liquefiable silty sands

94   that accumulated during the late Pleistocene and Holocene, that lies on the buried external portions

95   of the Apennine chain, where seismically active fault-fold structures exist (Toscani et al. 2009;

96   Minarelli et al. 2016), as shown in Figure 1. Besides the local stratigraphy, where the groundwater

97   table depths in February 2018 (GWT1) and April 2018 (GWT2) are also drawn, Figure 1 shows the

98   results of Cone Penetration Testing (CPT) carried out before and after RAP, the soils map and the

99   map of depth to groundwater table in Emilia-Romagna. More information can be found in Amoroso

100   et al. (2020a). The 6.1 M_w 2012 Emilia-Romagna earthquake, which involved a portion of this

101   region and caused the main damages in Ferrara and Modena provinces (Pondrelli et al. 2012), led to

102   liquefaction and sand boils geographically distributed along fluvial sand deposits (Tonni et al. 2015;

103   Amoroso et al. 2020b).

104   The experimental area (Figure 2) was an almost rectangular portion of a plowed field, with

105   sides of about 40 m and 80 m respectively. For the sake of brevity, the area is called the Region of

4

Interest (ROI). The field was not completely flat because several clods of soil give an irregular and jagged morphology. Two zones of the ROI, named the Natural Panel (NP) and Improved Panel (IP) respectively, were armed with an array of underground sequentially detonatable charges, in eight blast holes spaced around the perimeter of a circle (10 m diameter). The charges installation and detonation induced liquefaction in the silty sand from 3.5 to 9.5 m below the ground surface. The RAP columns were drilled from the surface up to 9.5 m depth in the IP area (Figure 2). On the contrary, the NP was left in its natural state. The distance between IP and NP was about 20 m, supposed to be long enough to exclude (or to significantly reduce) a possible interaction between blast effects and to support the hypothesis of same geotechnical soil properties and characteristics. Since a quality test revealed that a few RAPs in the upper-left part of IP had a reduced effectiveness due to their construction procedures (see further details in Amoroso et al., 2020a), some main effects are expected in that localized area of IP.

For convenience, the terms B0, B1 and B2 indicate the three stages of the experiment; B0 is the condition before blasts, while B1 and B2 represent conditions after the first (in the NP area) and the second blast (in the IP area), respectively. Subsequently, B1b refers to the stage immediately preceding the second blast, i.e. a stage in which temporary effects could still be present due to a not yet completed phenomenon exhaustion. Other technical details about the experiment can be found in Amoroso et al. (2020a), where each stage of the blasting is carefully described. As mentioned above, the acquisition of accurate information about surface variations (meaning primarily liquefaction-induced subsidence) was carried out by means of two independent remote sensing techniques: TLS and UAS-based SfM, as in Pesci et al. (2018). Table 1 summarizes the test scheduling. It should be noted that, given the limited time available, only a UAS survey was carried out at B1b stage.

Ten Ground Control Points (GCPs), evenly distributed on the ROI with positions provided by GNSS (Global Navigation Satellite System) measurements, were installed for georeferencing

131   scopes. Each GCP consisted of a target composed of two wooden arms 40 cm long forming a cross

132   shape, fixed to the ground. Finally, 62 survey stakes driven about 30 cm into the ground along a line

133   passing throughout the IP and NP centers allowed levelling measurements during the experiment

134   stages, leading to time series of the relative heights variations of the upper subsoil layer. The error

135   on stakes height measurement is ~1 mm, while the horizontal coordinates from rapid-static GNSS

136   observations are characterized by ~1 cm error.

137

138   **Remote sensing surveys and conventional ground settlement surveys**

139   The procedure for data analysis consisted of some steps: creation of point clouds; generation of the

140   corresponding Digital Terrain Models (DTMs), i.e. 2.5D models, from the point clouds; comparison

141   between DTMs; mapping and interpretation of terrain variations. DTMs comparisons provided

142   well-defined patterns of surface subsidence and terrain changes. In addition, conventional levelling

143   surveys taken before and after blasts provided very accurate time series of punctual height

144   variations along a reference line passing through NP and IP. These measurements were also useful

145   for constructive criticism about remote sensing results.

146

147   *TLS surveys*

148   TLS is a very efficient technique in surveying aimed at evaluating soil subsidence because of the

149   high spatial resolution, good accuracy and very low scans registration error, on condition that

150   suitable viewpoints are chosen (see e.g. Benito-Calvo et al. 2018). A Teledyne Polaris instrument

151   (Teledyne 2021), equipped with an electronic level to provide correct verticality, was mounted on a

152   pole at about 6 m above the ground, using a Level Lift Roof device (Scan&Go 2021) and acquired,

153   for each session, three scans, one for each of three viewpoints along a side of the ROI 40 m long

154   (Table 1 and Figure 3). The acquisition time for each scan was about 5 minutes, leading to a dense

155   point cloud with 5 mm sampling step at 100 m reference distance. The point clouds alignment by

means of the surface matching algorithm implemented in PolyWorks software package (Innovmetric 2021), led to three multitemporal point clouds. Subsequently, the data registration into the WGS84 UTM32 reference was carried out by means of GCP coordinates.

Figure 3 shows the complete point cloud acquired before the experiment and the point clouds specifically related to the ROI, i.e. the previously mentioned rectangular study area, for each experiment stage (B0, B1 and B2) subsequently used for data analysis.

Figure 4 shows the comparison between multitemporal TLS models. In particular, the differences B1-B0, B2-B0 and B2-B1 are presented in different forms by changing the scale to gradually describe the results from both the qualitative and quantitative point of view. The rows in Figure 4 describe the results using different scales to better point out both the variations and their planimetric distribution. Since the aim is to highlight the boundaries of the deformed zones and their spatial distribution as effect of blast-induced subsidence, only the areas with negative variations are shown. In the first row there are the maps of differences Δ in the range from 0 to -2 mm. In the other rows, the maximum settlement is progressively increased by ranges of 2 cm.

Some results can be directly inferred from Figure 4: 1) the subsided area of the NP is almost circular, showing main negative values (settlement) up to about 10 cm; 2) less marked lowering reveals the presence of ejected material; 3) the IP settlement pattern is not likewise regular and shows smaller maximum values (less than 6 cm) mainly distributed in a very localized top-left part of the area because of the reduced RAP effectiveness of some piers. This fact is also independently confirmed by geoelectric surveys performed soon after the blast, that identified more significant resistivity reduction in the upper-left piers in comparison to the surrounding IP soil (Amoroso et al. 2020a); 4) regarding the B2-B1 differences, a small settlement of ~2.5 cm in the area around the NP is evidenced around the circle; 5) there is noise in B1-B0 and B2-B1 maps consisting in a range of lines, which seem to radiate from a point in the NW part of the ROI, due to a strong wind event that

7

180   occurred during the second TLS survey (i.e. B1) and caused vibrations of the pole on which the

181   scanner was installed.

182   A morphological map is here defined as the difference between a point cloud and a reference

183   horizontal plane whose elevation is the mean elevation of that point cloud. Figure 5 shows the

184   complete information, i.e. the map of differences (B2-B0) and the morphological maps (B0 and B2)

185   with the same reference plane. The cumulative surface settlement map (B2-B0) allows the

186   recognition and quantification of a clear subsidence "bowl" in the area around the explosive

187   charges, with a lowering of about 6-8 cm widely distributed in the NP zone. After the second blast,

188   a few small zones in the IP area show maximum settlements ranging from 4 to 5 cm. In particular,

189   no more than 25% of the IP surface area shows significant changes, i.e. changes exceeding 4 cm,

190   confirming the effectiveness of the RAP-based liquefaction mitigation.

191   The procedure for volume computation requires some steps. At first, only point clouds parts

192   belonging to the deformed areas are used and modelled. For each model, a relative volume is

193   computed with respect to a reference horizontal plane. Subsequently, the pair-by-pair volume

194   differences lead to the results. Table 2 summarizes these results, including the settlement surface

195   areas, i.e. 375 m^2 and 420 m^2 for NP and IP, respectively. The apparently anomalous fact that the

196   reference area is slightly smaller (difference ~10%) in the case of NP panel is due to the presence of

197   equipment partially obstructing this zone and that must be removed from the point cloud before the

198   calculations. As expected, a noticeably smaller volume change characterizes the IP area.

199   The estimation of volume uncertainties come from an independent computation in areas not

200   affected by deformation providing an error-coefficient for unit area. The method runs by computing

201   volumes and volume differences with respect to a reference frame in a large portion of the ROI not

202   affected by blasts. In this case, the volume difference is 1.57 m^3 in an area of about 980 m^2, leading

203   to 0.0016 m^3 for unit area and, therefore, the uncertainties shown in Table 2.

204   A further computation of volume changes, carried out with the same approach, refers to two

205   smaller circular areas around blast centers having 7.5 m radius and provides -3.4 ± 0.3 m^3 in NP and

206   -1.6 ± 0.3 m^3 in IP. They represent, respectively, about 30% and 20% of the whole volume changes

207   previously computed. These values confirm that variations in IP are no more than 50% the one in

208   NP. However, a correction is necessary for the presence of extruded materials in NP (typically mud

209   cones) causing an underestimation of volume loss by subsidence. Inspecting point clouds and

210   isolating/removing materials deposited on the surface, highlight a volume underestimation of 0.9 ±

211   0.3 m^3. Therefore, the correct volume variation in NP is -4.3 m^3 instead of -3.4 m^3. The results

212   show that, in terms of volume changes, the effects detected in IP were no more than about 37% of

213   those in NP, corresponding to a 63% mitigation factor.

214

215   *SfM surveys*

216   SfM surveys were carried out by means of an UAS equipped with a DJI FC6310 camera and flying

217   at about 20 m above the ground. The main technical specifications for the camera, including the

218   GSD at 20 m flight height, are summarized in Table 3.

219   The drone flew four times in the time span from 10:00 to 16:00 (Table 1): the first time before

220   blast (B0); the second one after the first blast (B1); the third one about two hours after B1 (B1b);

221   the last one after the second blast (B2). For each flight, about 60 images were taken and processed

222   by means of the PhotoScan software package, now upgraded in Metashape (Agisoft 2021), leading

223   to the point clouds shown in Figure 6. It is interesting to note that SfM allows the recognition of the

224   effects of groundwater leakage (bluish areas in Figure 6). A completely free approach to bundle

225   adjustment was used, i.e. no GCPs were used to carry out the photogrammetric modeling. The

226   image alignment was based on full-size images, without subsampling, by choosing the option 'High

227   accuracy' in PhotoScan.

228   The 'High' option for dense cloud generation was selected in the last step of SfM processing,

229   resulting in point clouds having 5 mm sampling step. Figure 7 provides details about the blast areas,

230   pointing out local changes, mainly attributable to mud volcanoes, emissions of water, sand and silt.

231   Note that the availability of a model related to an inter-blast time, i.e. B1b, allows the detection of

232   variations observed after a few hours in comparison to rapid soil settlement shortly after the

233   liquefaction and pore pressure dissipation.

234   The maps of differences were created following the same approach used for the TLS data

235   analysis. The comparison between Figures 6 (SfM) and 4, 5 (TLS) shows that the same magnitudes

236   and similar patterns of subsidence were obtained. The difference maps from SfM show greater

237   subsidence in the NP area with respect to the IP where RAP installation reduced settlement both in

238   space distribution and maximum subsidence. The quite similar maps from B1b-B1 and B2-B1 seem

239   to ensure that there are no significant interactions between blasts, suggesting that 20 m distance was

240   an appropriate choice, even if this assertion comes from surficial measures only. Finally, the TLS

241   and SfM point clouds were registered into the same relative reference frame by means of surface

242   matching algorithms applied to the part of the ROI far from the blasting areas. In particular, the use

243   of targets for the registration into an external reference frame was unnecessary in this stage.

244

245   *Levelling and cross-sections*

246   Ground surface settlements for the first (B1) and the second (B2) blasts, based on the elevation

247   change of the survey stakes, are plotted in Figure 8 along the line through the NP and IP centers.

248   The automatic level used to for measurements was located about 20 m from the blast center,

249   preventing liquefaction-induced settlement. Levelling measures were taken after 30-60 minutes

250   from blasts, when excess pore pressure had probably almost fully dissipated. Reconsolidation

251   following the blast-induced liquefaction produced a nearly symmetrical settlement pattern across

252   the NP as shown in Figure 8 for the first blast. Maximum settlement at the center of the blast ring

253 was ~9.5 cm and settlement decreased to zero at a distance of ~12 m from this center. Settlements

254 within the blast ring were between 7.0 and 9.5 cm after the first blast.

255   The second blast produced both settlement within the IP area and some minor additional

256 settlement in the NP one, possibly due to strain softening during the first blast sequence. The IP

257 surface settlement due to the second blast was significantly lower than the one occurred in NP area

258 as effect of the first blast. However, the settlement profile around the IP was not symmetric, as

259 observed in the NP for B1, but was higher on the north side where the RAPs were characterized by

260 lower quality, as already discussed. This result is consistent with observations from the TLS and

261 SfM surveys.

262   A Sondex profilometer pipe placed at the NP and IP centers provided the measurements of

263 settlement as a function of depth. The results show that liquefaction-induced variations primarily

264 occurred between 3.5 and 11.0 m below the ground surface. Moreover, there is agreement between

265 the measured surface and subsoil settlements.

266

267 **Crossline inspection**

268 The availability of 62 survey stakes placed on the line connecting the blast centers allowed a

269 comparison between remote sensing and classical levelling data. As mentioned in section devoted

270 to the study site description, the horizontal coordinates of the stakes were obtained by means of

271 GNSS observations. WGS84 UTM32 reference frame was used. Moreover, the relative height of

272 the head of each stake was measured three times (before the test, after the first blast and after the

273 second blast).

274   To provide a direct comparison between TLS/SfM data and levelling data, the georeferenced

275 TLS point clouds are used. However, for a better representation and description, the data are given

276 in an arbitrary reference frame where the x-axis is the line joining the blast area centers, the z-axis is

277 vertical and the y-axis is defined accordingly (Figure 9). Actually, two cross-sections, named A and

11

278 B respectively, were extracted from each one of the TLS point clouds on two parallel lines 0.5 m on

279 opposite sides of the stake line. This was necessary because of the presence of stakes noising and

280 obstructing the surface. Moreover, the used remote sensing techniques do not allow the repeated

281 measurement of the same specific point but leads to the acquisition of point clouds distributed on

282 the observed areas.

283   Figure 9 illustrates the lines of the cross-sections drawn on the ROI and the cross-sections,

284 extracted with 5 cm sampling test, related to all the point clouds. Figure 10 shows the cross-sections

285 related to NP and IP areas. Finally, Figure 11 shows the height differences computed along the A

286 and B cross-sections for the three stages, which constitute the significant information about the

287 blast-induced changes.

288   TLS and levelling measure different objects. The first one provides points distributed on the

289 surface, the second one measures the head of stakes at a certain height above surface and stakes are

290 connected to the subsoil at about 30 cm depth. Therefore, a direct comparison between TLS and

291 levelling data is not possible. For this reason, TLS and levelling comparison refers to heights

292 variations, even if the changes due to material accumulation on the ground cannot be measured by

293 levelling.

294   Figure 12 shows TLS and levelling data over-imposed. The points extracted from DTMs (the

295 cumulative surface variation, i.e. B2-B0, as indicated in previous figures) along the cross-section A

296 and B profiles are shown together with the points provided by the level survey (STi). The

297 agreement is quite good despite the presence of some interesting differences. A simple statistics

298 allows the quantification of discrepancies between the two data sets. Figure 12 also shows a

299 histogram with the frequency of differences between TLS and STi data. The difference with the

300 highest frequency is -2 mm with a standard deviation (SD) of 8 mm. However, there is also a

301 secondary peak with a mean value of -21 mm with 6 mm SD. Both the distributions appear to have

302   almost Gaussian shape. Note that data for statistics from TLS cross-sections were interpolated at the

303   same sampling step of levelling to use compatible data set distribution.

304   Some differences are clearly due to the presence of ejected material but the offset between

305   TLS and levelling is also present in the near around of IP and NP areas. The farther from the centre

306   the less discrepancy. These fact should be taken into account for the result interpretation: (1) the

307   stakes are inserted into the ground, therefore they are connected to a deeper layer, more compacted

308   than the superficial plowed terrain; (2) the extruded material cannot be observed by measuring the

309   top of stakes but accumulate at the ground surface; (3) the levelling and TLS lines does not coincide

310   spatially despite are very close (as above described, the cross-sections where taken at 0.5 m from

311   the levelling line); (4) some errors in points positioning the STi into TLS reference frame could be

312   possible due to the alignment of different frames.

313

314   **Discussion**

315   The main objectives of this study are: (1) to evaluate the quality and significance of the remote

316   sensing measurements aimed at studying the settlement of the soil surface due to earthquake-

317   induced or blast-induced liquefaction, and (2) to quantitatively assess the reduction in settlement

318   allowed by the RAP-related mitigation of the liquefaction hazard.

319   The maps of differences provided by TLS and SfM at the various stages of the experiment

320   provided the same qualitative and quantitative results. In particular, the deformations patterns

321   visible in the NP and IP areas, which correspond to a natural and a treated site respectively, are

322   significantly different. It is important to underline that remote sensing techniques allow a

323   characterization of the soil surface over the entire study area, highlighting localized phenomena that

324   may not be captured by other observation methods such as levelling. Moreover, TLS and SfM allow

325   very fast surveys. Therefore, these techniques are sufficient to characterize the deformation

326   patterns, leading to very dense point clouds suitable for both qualitative and quantitative

evaluations. Note that the photogrammetric modeling was implemented with free-net bundle adjustment, i.e. the GCPs were used for the sole purpose of georeferencing the point cloud and provide, at the same time, the correct scale factor. On the other hand, although PhotoScan (or Metashape) allows the use of GCPs to constrain the bundle adjustment, not all photogrammetric software packages allow this. If a planar surface is observed from a large number of viewpoints well distributed in space, which is the case of the surface surveyed in this test, the constraint by GCPs is unnecessary.

The comparison between TLS and levelling data highlighted peculiarities related to the fact that remote sensing techniques only provide data about the soil surface. This comparison, characterized by a very high precision in height measurement (~1 mm), showed a not negligible discrepancy. This suggests that measured surficial deformation could underestimate the real settlements up to ~15%, probably due to a weak connection between surface and underlying layers. Note that the experimental field is an agricultural context and the ground is periodically moved and plowed and treated resulting in a set of loose soil elements.

These discrepancies suggest that in some specific environment the results from remote sensing require a little bit criticism for interpretation, especially in the case of data relating to agricultural areas. Although this evidence is limited to this case study only, it is to consider that data provided by Synthetic Aperture Radar (SAR) from satellite or other terrestrial, airborne or satellite remote sensing techniques are used to provide the ground deformation at regional scale, in particular the effects of liquefaction, due to a seismic event (see e.g. Chini et al. 2015). This should be taken into account both in the generation of a 3D displacement field from a 2D one (see e.g. Fernandez et al. 2018) and in the study of a numerical model that aims to reconstruct motions in depth at the fault level starting from the 2D displacement field on the ground surface (Currenti et al. 2010).

351   Regarding the geotechnical aspects of the described blast test, the settlement occurred in the

352   NP resulted in a bowl-shaped settlement pattern over a wide area leading to subsidence of up to 10

353   cm. This settlement was accompanied by the ejection of water and sands from subsoil. In contrast,

354   in the IP area the effects were quite reduced, involving a smaller portion of the area and only

355   subjected to a few centimeters of subsidence. In particular, no more than 25% of the IP area was

356   affected by settlement greater than 6 cm and this appears to be an area where the RAP installation

357   was poorly performed. Moreover, almost no ejection of sand or water occurred in such an area. This

358   reduction in ejecta produced by the RAP group is significant considering that ejecta is estimated to

359   have been responsible for more than 33% of the damage in the Christchurch New Zealand

360   earthquake sequence (Quigley et al. 2013).

361   Finally, the precision of TLS and SfM data was adequate for a complete characterization of

362   the ground settlement variations for both NP and IP areas. The results also showed that TLS and

363   SfM can provide reliable volume calculations, including an estimation of the volume of the ejected

364   material. In particular, the results highlighted that the subsidence in areas improved by RAP was

365   meanly reduced by a factor 50%. In the area where the RAP-based improvement was greater, the

366   volume change did not exceed 37% of that in the non-improved area.

367

368   **Conclusions**

369   Performance and limits of TLS and SfM for the characterization of the ground surface deformation

370   of silty sand areas affected by earthquake-induced liquefaction were studied in controlled

371   conditions thanks to a blast test. In particular, an untreated natural (NP) area and an area treated

372   with a group of RAPs for improved liquefaction resistance (IP) were studied before the test, after a

373   first blast in the NP area and after a second blast in the IP area.

374   The maps of settlement difference provided by TLS and SfM were qualitatively and

375   quantitatively coherent. These remote sensing techniques showed that the settlement in the NP area

376 was widely distributed over a large area, with maximum subsidence of ~10 cm, whereas in the IP a

377 smaller area was affected by of 5 to 6 cm subsidence. Besides some interesting advantages of TLS

378 and SfM, including the rapidity of data acquisition and processing, also a problem must be taken

379 into account. The deformation obtained from these remote sensing techniques could sometimes

380 underestimate the real subsidence effects up to about 15%, as the comparison with the levelling

381 survey pointed out. These evidences from this specific study case cannot be exported as a general

382 result but indicate that a carefully criticism is needed in data interpretation instead. They will be

383 useful in planning the next blast test scheduled for 2021 in a new test site in Emilia-Romagna. The

384 results showed that, despite this systematism, remote sensing techniques allowed reliable volume

385 calculations and, in particular, highlighted the RAP performance.

386

387 **Data Availability Statement**

388 Some or all data, models, or code that support the findings of this study are available from the

389 corresponding author upon reasonable request. The available data are: all images, all point clouds,

390 all PhotoScan and PolyWorks projects.

391

401   Andrea Carpena for the services and for the aerial images; Teledyne (Dario Conforti), Scan&Go srl

402   (Massimo Secchia) and iMages SpA (Donato Marcantonio) for their invaluable help in laser

403   scanning monitoring; Fawzi Doumaz (INGV) for flight organization and UAV images; Michele

404   Perboni, who kindly guested the experimental activities, Bondeno Municipality (in particular

405   Stefano Ansaloni, Olga Mantovani and Elena Bonora) and   Emilia-Romagna Region (Luca

406   Martelli), who provided all the necessary support to realize the research in collaboration with the

407   other local authorities (Ferrara Prefecture, Ferrara Province, Local Civil Protection, Police).

408

409   **References**

410   Agisoft, 2021. "PhotoScan/Metashape web site." Accessed April 20, 2021. http://www.agisoft.com.

411   Amoroso, S., K.M. Rollins, P. Andersen, G. Gottardi, L. Tonni, M.F. García Martínez, K.

412   Wissmann, L. Minarelli, C. Comina, D. Fontana, D., et al., 2020a. "Blast-induced liquefaction in

413   silty sands for full-scale testing of ground improvement methods: Insights from a multidisciplinary

414   study." *Engineering Geolog*y 265: 105437. https://doi.org/10.1016/j.enggeo.2019.105437.

415   Amoroso, S., C. Comina, and D. Marchetti, 2020b. "Combined P- and S-wave measurements by

416   seismic dilatometer test (SPDMT): a case history in Bondeno (Emilia Romagna, Italy)."

417   *Geotechnical Testing Journal* 43: 2. https://doi.org/10.1520/GTJ20180233.

418   Amoroso, S., G. Milana, K. M. Rollins, C. Comina, L. Minarelli, M. R. Manuel, P. Monaco, et al.

419   2017. "The First Italian Blast-Induced Liquefaction Test (Mirabello, Emilia-Romagna, Italy):

420   Description of the Experiment and Preliminary Results." *Annals of Geophysics* 60 (5): S0556.

421   https://doi.org/10.4401/ag-7415.

422   Ashford, S.A., K.M. Rollins, and J.D. Lane, 2004. "Blast-Induced Liquefaction for Full-Scale

423   Foundation Testing." *Journal of Geotechnical & Geoenvironmental Engineering* 130 (8), 798-806.

424   https://doi.org/10.1061/(ASCE)1090-0241(2004)130:8(798).

425 Benito-Calvo, A., F. Gutiérrez, A. Martínez-Fernández, D. Carbonel, T. Karampaglidis, G. Desir, J.

426 Sevil, J. Guerrero, I. Fabregat, and Á. García-Arnay, 2018. "4D Monitoring of Active Sinkholes

427 with a Terrestrial Laser Scanner (TLS): A Case Study in the Evaporite Karst of the Ebro Valley, NE

428 Spain." *Remote Sensing* 10(4): 571. https://doi.org/10.3390/rs10040571.

429 Brunier, G., J. Fleury, J.E. Anthony, V. Pothin, C. Vella, P. Dussouillez, A. Gardel, and E.

430 Michaud, 2016. "Structure-from-Motion photogrammetry for high-resolution coastal and fluvial

431 geomorphic surveys." *Géomorphologie* 22 (2), 147–161.

432 https://doi.org/10.4000/geomorphologie.11358.

433 Chini, M., M. Albano, M. Saroli, L. Pulvirenti, M. Moro, C. Bignami, E. Falcucci, S. Gori, G.

434 Modoni, N. Pierdicca, and S. Stramondo, 2015. "Coseismic liquefaction phenomenon analysis by

435 COSMO-SkyMed: 2012 Emilia (Italy) earthquake." *International Journal of Applied Earth*

436 *Observation and Geoinformation* 39, 65-78. https://doi.org/10.1016/j.jag.2015.02.008.

437 Currenti, G., A. Bonaccorso, C. Del Negro, F. Guglielmino, D. Scandura, and E. Boschi, 2010.

438 "FEM-based inversion for heterogeneous fault mechanisms: application at Etna volcano by

439 DInSAR data." *Geophysical Journal International* 183, 765-733. https://doi.org/10.1111/j.1365-

440 246X.2010.04769.x

441 EN, 2004. *Eurocode 8: Design of Structures for Earthquake Resistance – Part 5: Foundations,*

442 *Retaining Structures and Geotechnical Aspects*. Bruxelles: CEN European Committee for

443 Standardization.

444 Fey, C., and V. Wichmann, 2017. "Long- range terrestrial laser scanning for geomorphological

445 change detection in alpine terrain – handling uncertainties." *Earth Surface Processes and*

446 *Landforms* 42, 789-802. https://doi.org/10.1002/esp.4022.

447 Fernandez, J., J.F. Prieto, J. Escayo, A.G. Camacho, F. Luzón, K.F. Tiampo, M. Palano, T. Abajo,

448 E. Pérez, J. Velasco, J., et al. 2018. "Modeling the two- and three-dimensional displacement field in

449 Lorca, Spain, subsidence and the global implications." *Scientific Reports* 8: 14782. https://doi.org/

450 10.1038/s41598-018-33128-0

451 Finno, R.J., A.P. Gallant, and P.J. Sabatini, 2016. "Evaluating Ground Improvement after Blast

452 Densification at the Oakridge Landfill." *Journal of Geotechnical & Geoenvironmental Engineering*

453 142 (1), 1-13. https://doi.org/10.1061/(ASCE)GT.1943-5606.0001365.

454 Giona Bucci, M., P. Villamor, P. Almond, M. Tuttle, M. Stringer, W. Ries, C. Smith, M. Hodge,

455 and M. Watson, 2018. "Associations between sediment architecture and liquefaction susceptibility

456 in fluvial settings: The 2010–2011 Canterbury Earthquake Sequence, New Zealand." *Engineering*

457 *Geology* 237, 181-197. https://doi.org/10.1016/j.enggeo.2018.01.013.

458 Gutiérrez, F., M. Zarroca, R. Linares, C. Roqué, D. Carbonel, J. Guerrero, J.P. McCalpin, X.

459 Comas, and A.H. Cooper, 2018. "Identifying the boundaries of sinkholes and subsidence areas via

460 trenching and establishing setback distances." *Engineering Geology* 233, 255-268. https://doi.org/

461 10.1016/j.enggeo.2017.12.015.

462 Győri, E., L. Tóth, Z. Gráczer, and T. Katona, 2011. "Liquefaction and Post-Liquefaction

463 Settlement Assessment – A Probabilistic Approach." *Acta Geodaetica et Geophysica Hungarica* 46

464 (3), 347-369. https://doi.org/10.1556/AGeod.46.2011.3.6.

465 Hu, J. and H. Liu, 2019. "Identification of ground motion intensity measure and its application for

466 predicting soil liquefaction potential based on the Bayesian network method." *Engineering Geology*

467 248, 34-49. https://doi.org/10.1016/j.enggeo.2018.11.006.

468 Innovmetric 2021. "PolyWorks web site." Accessed: April 20, 2021. https://www.innovmetric.com.

469 Minarelli, L., S. Amoroso, G. Tarabusi, M. Stefani, and G. Pulelli, 2016. "Down-hole geophysical

470 characterization of middle-upper Quaternary sequences in the Apennine Foredeep, Mirabello,

471 Italy." *Annals of Geophysics* 59 (5): S0543. https://doi.org/10.4401/ag-7114.

472 Pesci, A., G. Teza, V. Kastelic, and M.M.C. Carafa, 2020. "Resolution and precision of fast, long

473 range terrestrial photogrammetric surveying aimed at detecting slope changes." *Journal of*

Surveying Engineering 146 (4): 04020017-1-13. https://doi.org/10.1061/(asce)su.1943-5428.0000328.

Pesci, A., S. Amoroso, G. Teza, and L. Minarelli, 2018. "Characterisation of soil deformation due to blast-induced liquefaction by UAV-based photogrammetry and terrestrial laser scanning." *International Journal of Remote Sensing* 39 (22), 8317-8336. https://doi.org/10.1080/01431161.2018.1484960.

Pesci, A., G. Teza, and E. Bonali, 2011. "Terrestrial laser scanner resolution: numerical simulations and experiments on spatial sampling optimization." *Remote Sensing* 3 (1), 167-184. https://doi.org/10.3390/rs3010167.

Pondrelli, S., S. Salimbeni, P. Perfetti, and P. Danecek, 2012. "Quick regional centroid moment tensor solutions for the Emilia 2012 (northern Italy) seismic sequence." *Annals of Geophysics* 55 (4), 615-621. https://doi.org/10.4401/ag-6146.

Quigley, M.C., S. Bastin, and B.A. Bradley, 2013. "Recurrent liquefaction in Christchurch, New Zealand, during the Canterbury earthquake sequence." *Geology*, 41 (4), 419-422. https://doi.org/10.1130/G33944.1.

Rauhala, A., A. Tuomela, C. Davids, and P.M. Rossi, 2017. "UAV Remote Sensing Surveillance of a Mine Tailings Impoundment in Sub-Arctic Conditions." *Remote Sensing* 9: 1318. https://doi.org/10.3390/rs9121318.

Saftner, D.A., R.A. Green, and R.D. Hryciw, 2015. "Use of explosives to investigate liquefaction resistance of aged sand deposits." *Engineering Geology* 199, 140-147. https://doi.org/10.1016/j.enggeo.2015.11.002.

Scan&Go, 2021. "Level lift roof web site." Accessed April 20, 2021. https://www.scan-go.eu/product/level-lift-roof-evo/

497 Saftner, D.A., J. Zheng, R.A. Green, R. Hryciw, and K. Wissmann, 2018. "Rammed aggregate pier

498 installation effect on soil properties." *Institution of Civil Engineers-Ground Improvement* 171 (2),

499 63-73. https://doi.org/10.1680/jgrim.16.00021

500 Smith, M.W., J.L. Carrivick, and D.J. Quincey, 2016. Structure from motion photogrammetry in

501 physical geography. *Progress in Physical Geography* 40 (2), 247-275. https://doi.org/

502 10.1177/0309133315615805.

503 Teledyne, 2021. "Teledyne Polaris laser scanning website." Accessed April 20, 2021.

504 https://www.teledyneoptech.com/en/products/static-3d-survey/polaris/

505 Tonni, L., G. Gottardi, S. Amoroso, R. Bardotti, I. Bonzi, A. Chiaradonna, A. d'Onofrio, V.

506 Fioravante, A. Ghinelli, D. Giretti, et al., 2015. "Interpreting the deformation phenomena triggered

507 by the 2012 Emilia seismic sequence on the Canale Diversivo di Burana banks." *Italian*

508 *Geotechical Journal* 49 (2), 28-38.

509 http://www.associazionegeotecnica.it/sites/default/files/rig/2_2015_028ton.pdf.

510 Toscani, G., P. Burrato, D. Di Bucci, S. Seno, and G. Valensise, 2009. "Plio-Quaternary tectonic

511 evolution of the northern Apennines thrust fronts (Bologna-Ferrara section, Italy): seismotectonic

512 implications." *Italian Journal of Geosciences* 128, 605-613.

513 https://doi.org/10.3301/IJG.2009.128.2.605

514 Vosselman, G., and H.G. Maas, eds. 2010. *Airborne and terrestrial laser scanning*. Boca Raton FL:

515 CRC Press.

516 Wentz, F.J., S. van Ballegooy, K.M. Rollins, S.A. Ashford, and M.J. Olsen, 2015. "Large Scale

517 Testing of Shallow Ground Improvements Using Blast-Induced Liquefaction." Paper presented at

518 the 6th International Conference on Earthquake Geotechnical Engineering (6ICEGE), Christchurch,

519 NZ, November 1-4. Accessed April 20, 2021.

520 https://secure.tcc.co.nz/ei/images/ICEGE15%20Papers/Wentz_530.00.pdf.

521

Table 1

Table 1. Test scheduling. Times refer to Central European Time (CET), i.e. Coordinate Universal Time + 1h.

Event	Pre-blast	First blast [a]	Inter-blast		Second blast [b]	Post-blast
TSL survey [c]	11:00 (B0)	---	12:50 (B1)	---	---	16:00 (B2)
UAV flight [c]	10:10 (B0)	---	12:40 (B1)	15:05 (B1b)	---	15:50 (B2)
Blast [d]	---	12:15	---	---	15:30	

[a] blast in NP area

[d] blast in IP area

[c] Times at mean survey

[d] Actual times

Table 2

Table 2. Volume variations due to blasts in NP and IP areas.

Case	ΔV (m^3)	
	NP [a]	IP [b]
B2-B0	-12.5 ± 0.7	-6.3 ± 0.6
B1-B0	-11.3 ± 0.7	0.8 ± 0.6
B2-B1	-1.3 ± 1.0	-7.1 ± 0.8

[a] Reference area: 375 m^2

[b] Reference area: 420 m^2

Table 3

Table 3. Main camera technical specifications and image parameters.

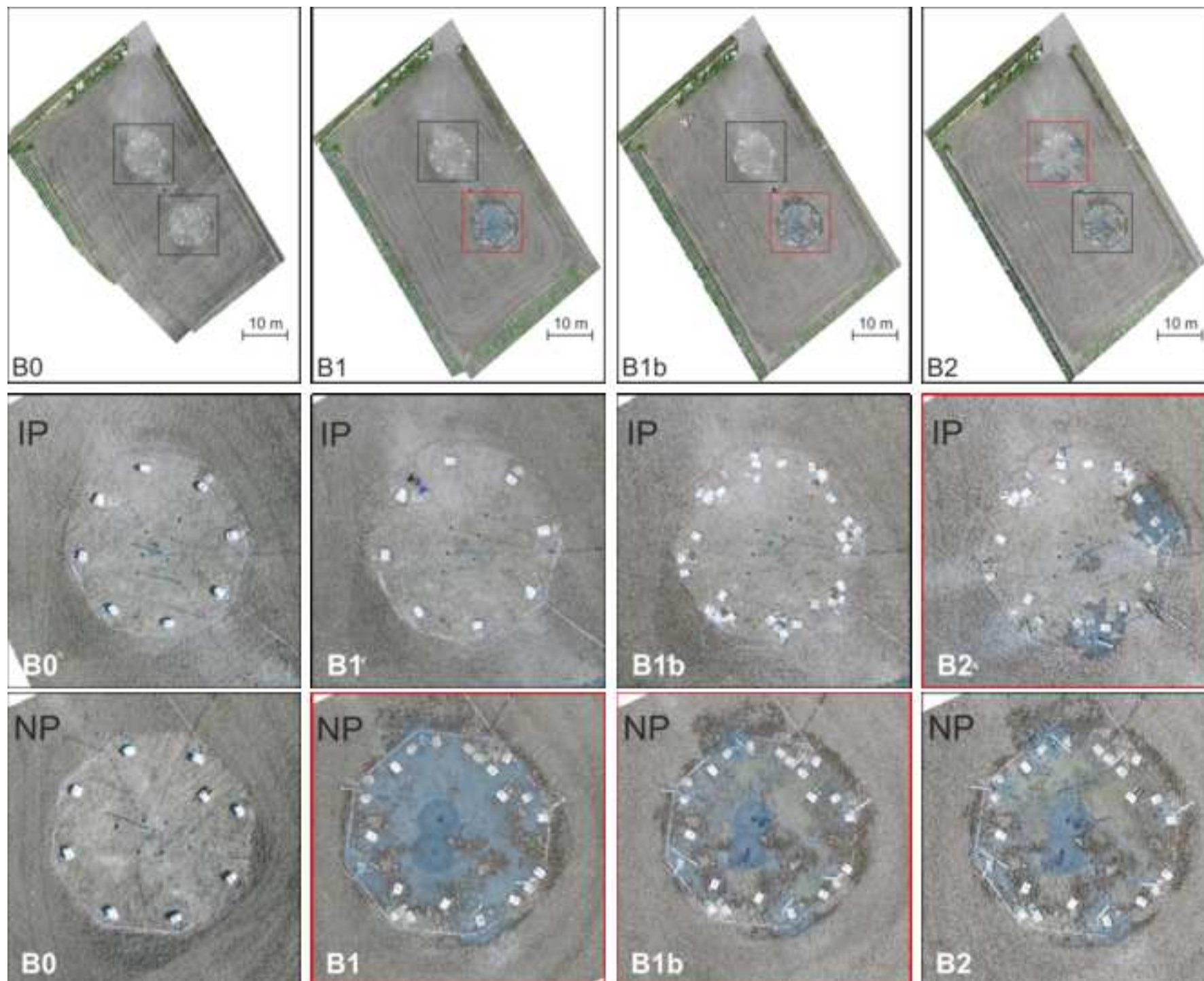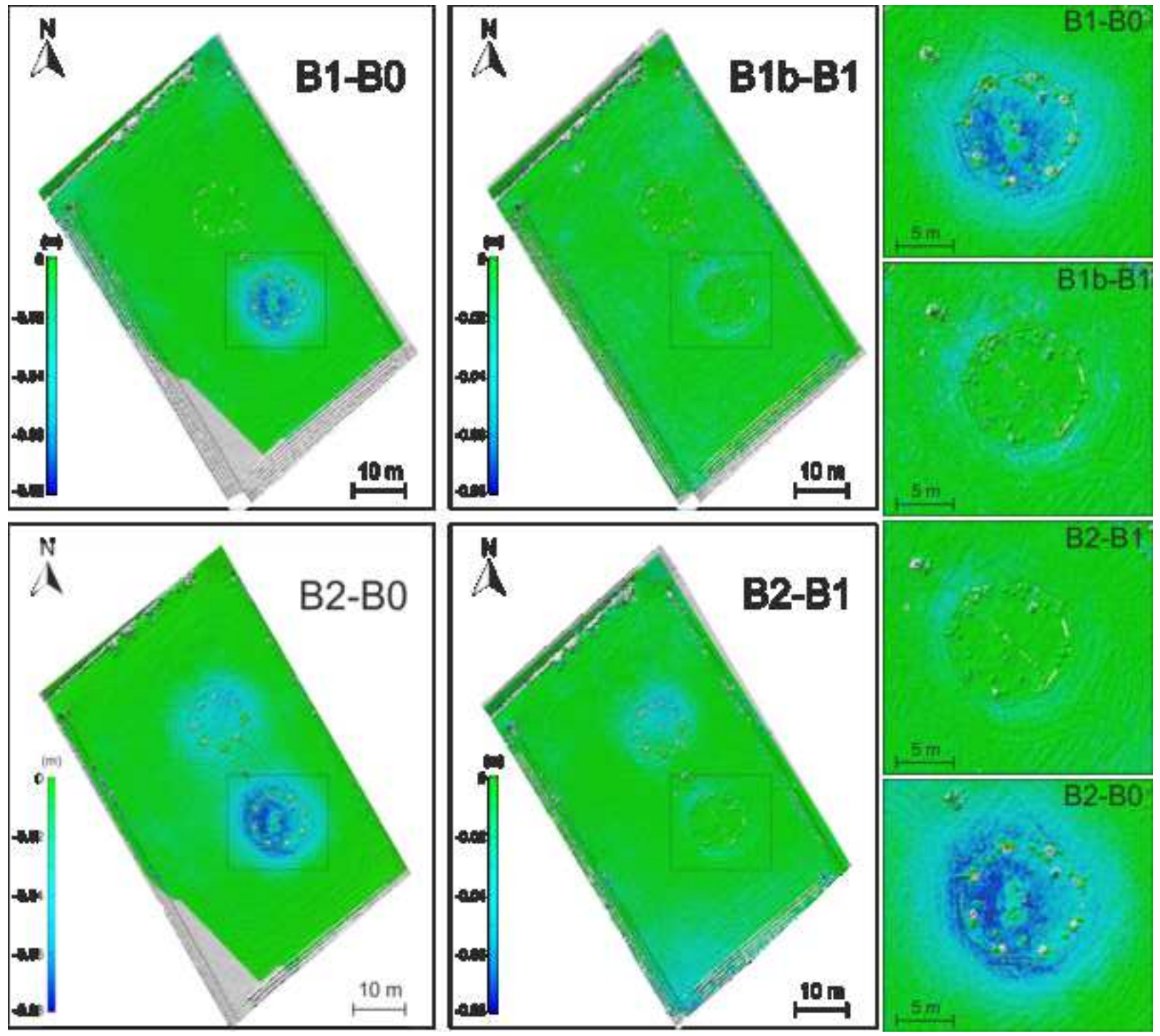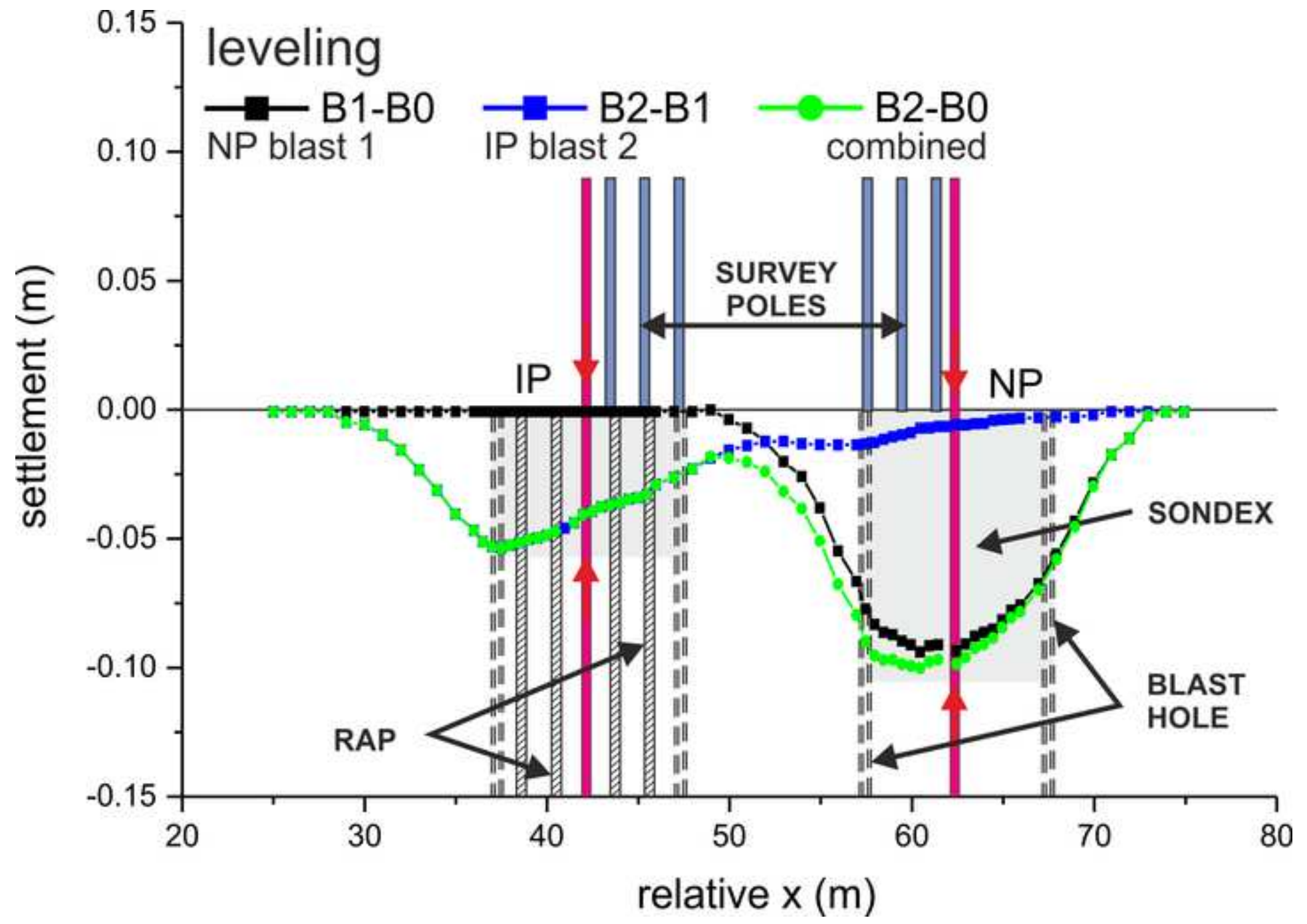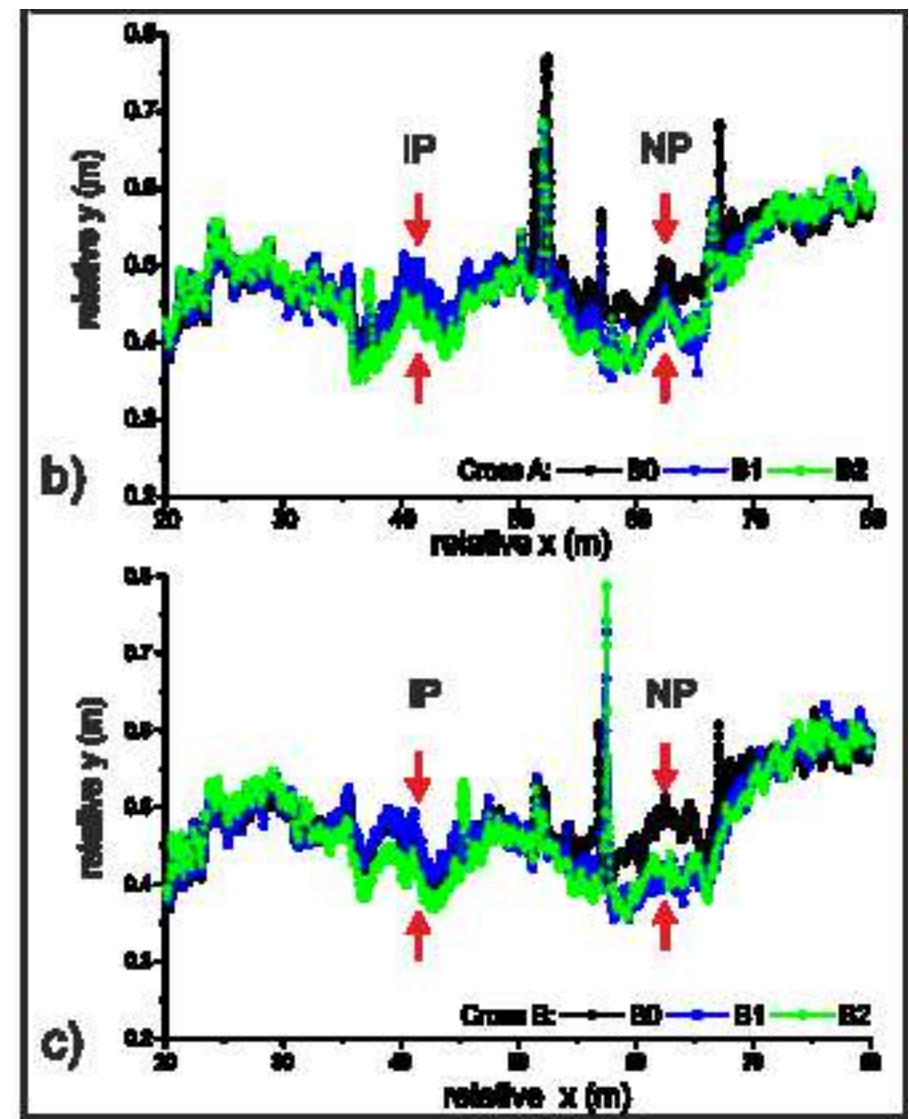| Feature/parameter	Unit	DIJ FC6310
Focal length	mm	8.8
Aperture (f-stop)	-	f/5.6
Equivalent focal length 35 mm	mm	24
Crop factor	-	2.7
Sensor number of pixels	-	5472×3648
Sensor size	mm × mm	13.2×8.8
Pixel side	mm	0.00241
Exposition time	S	1/400
GSD at 20 m flight	mm	5.5

Figure 1

Click here to access/download;Figure;Fig1.tif

Figure 2

Figure 4　Click here to access/download;Figure;FIG4 NEW.tif ⬇

Figure 5

Figure 6

Click here to access/download;Figure;FIG6 NEW.tif

Figure 7

Figure 8   Click here to access/download;Figure;Fig8.tif ⬇

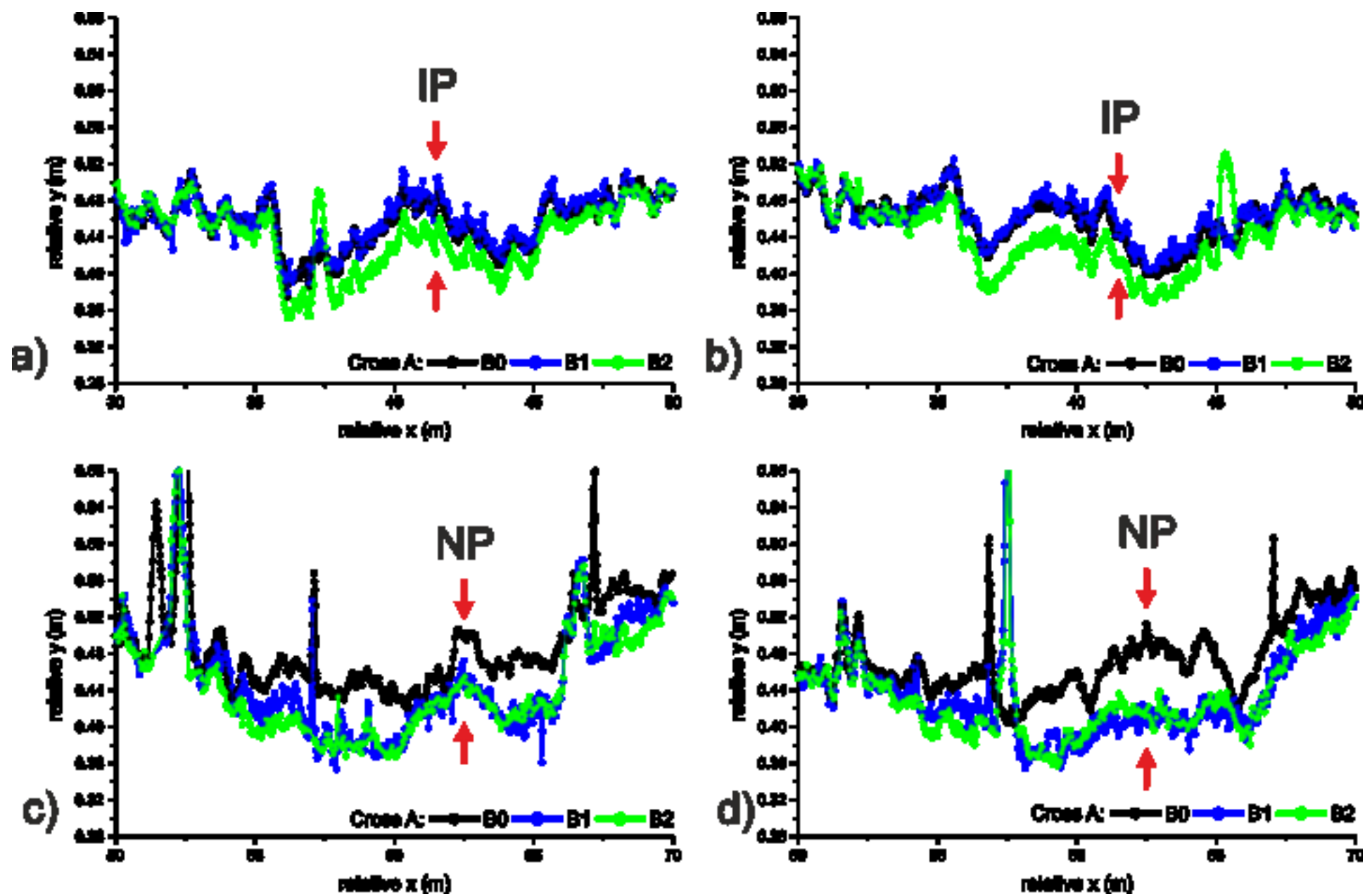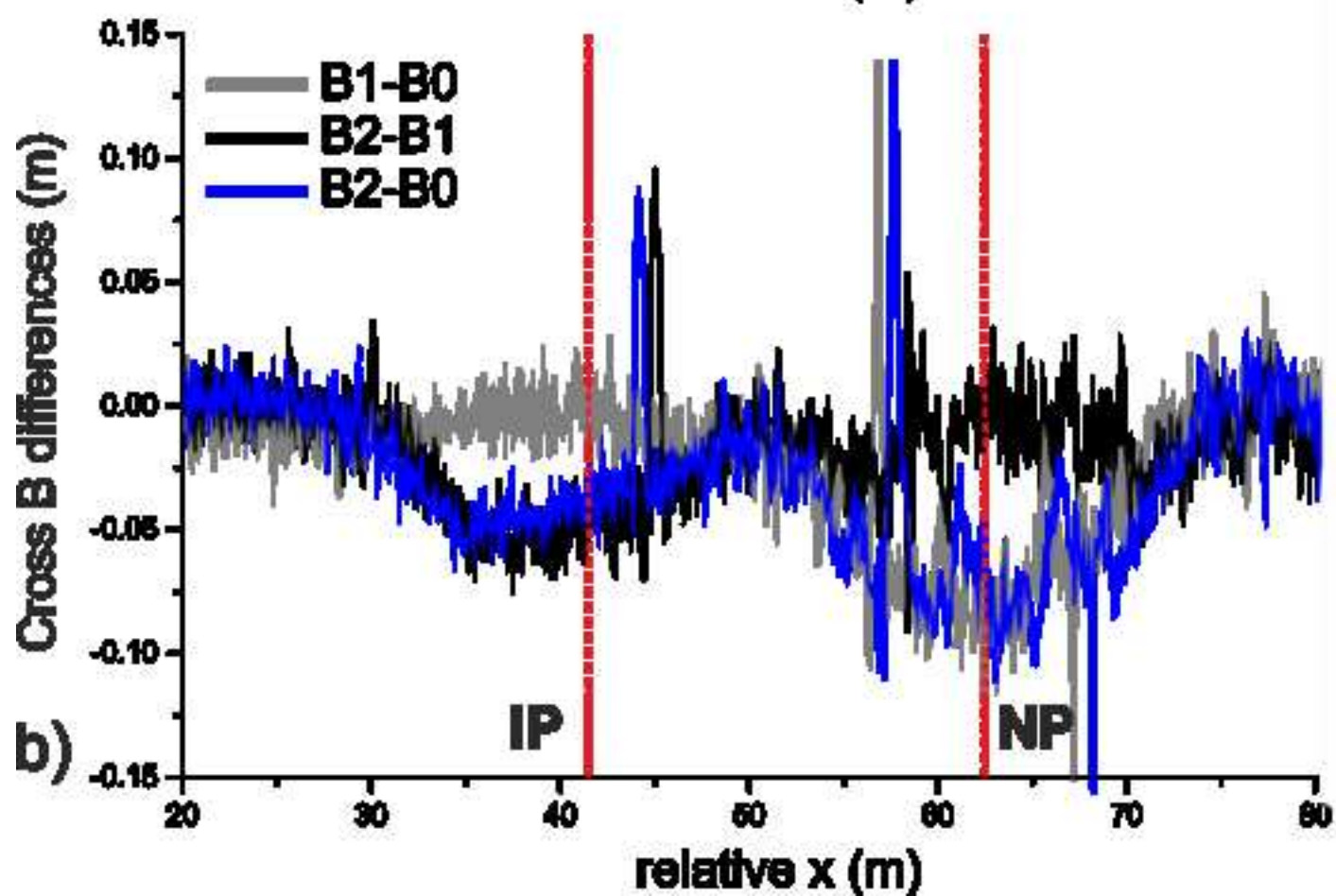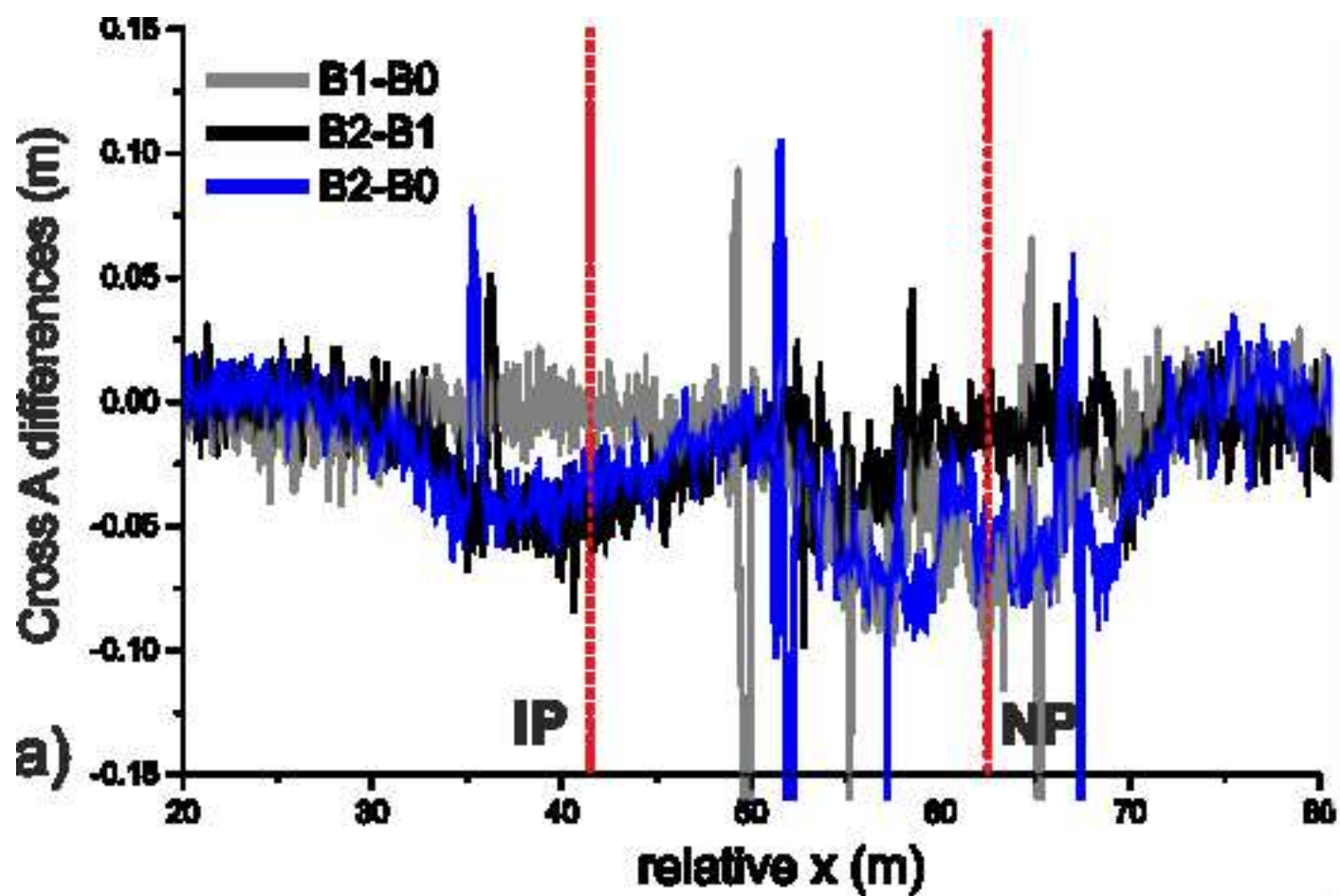Figure 9   Click here to access/download;Figure;FIG9 NEW.tif
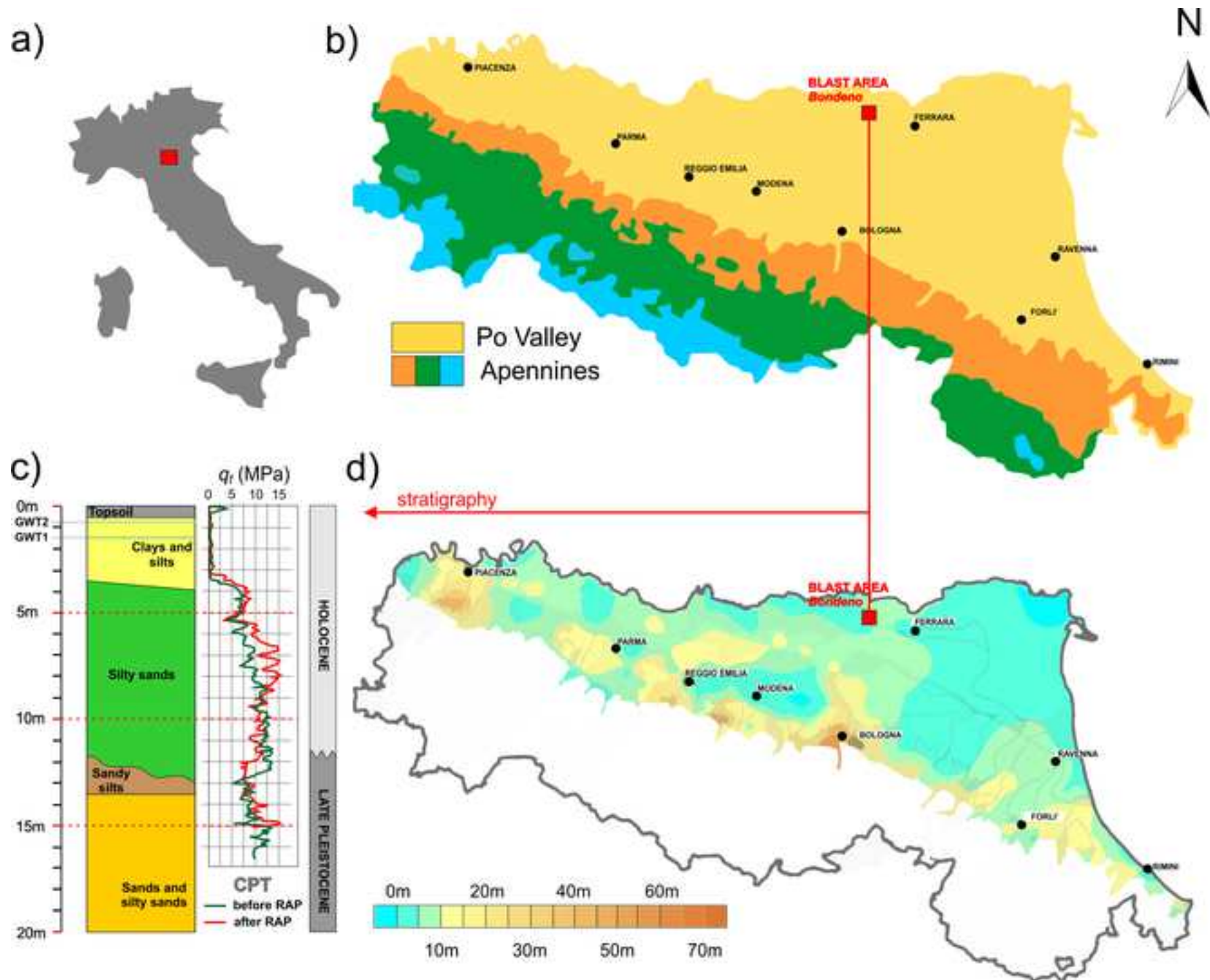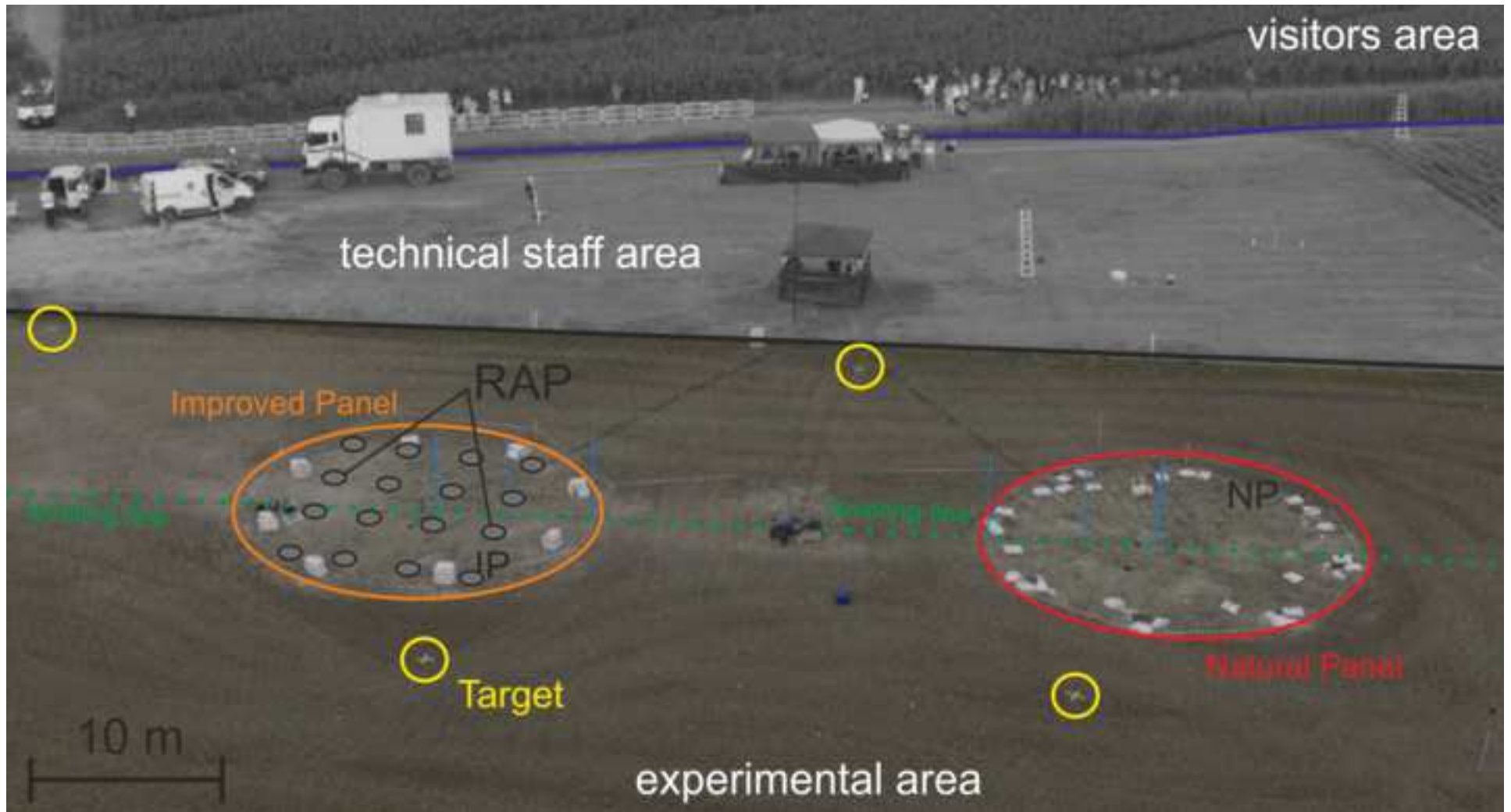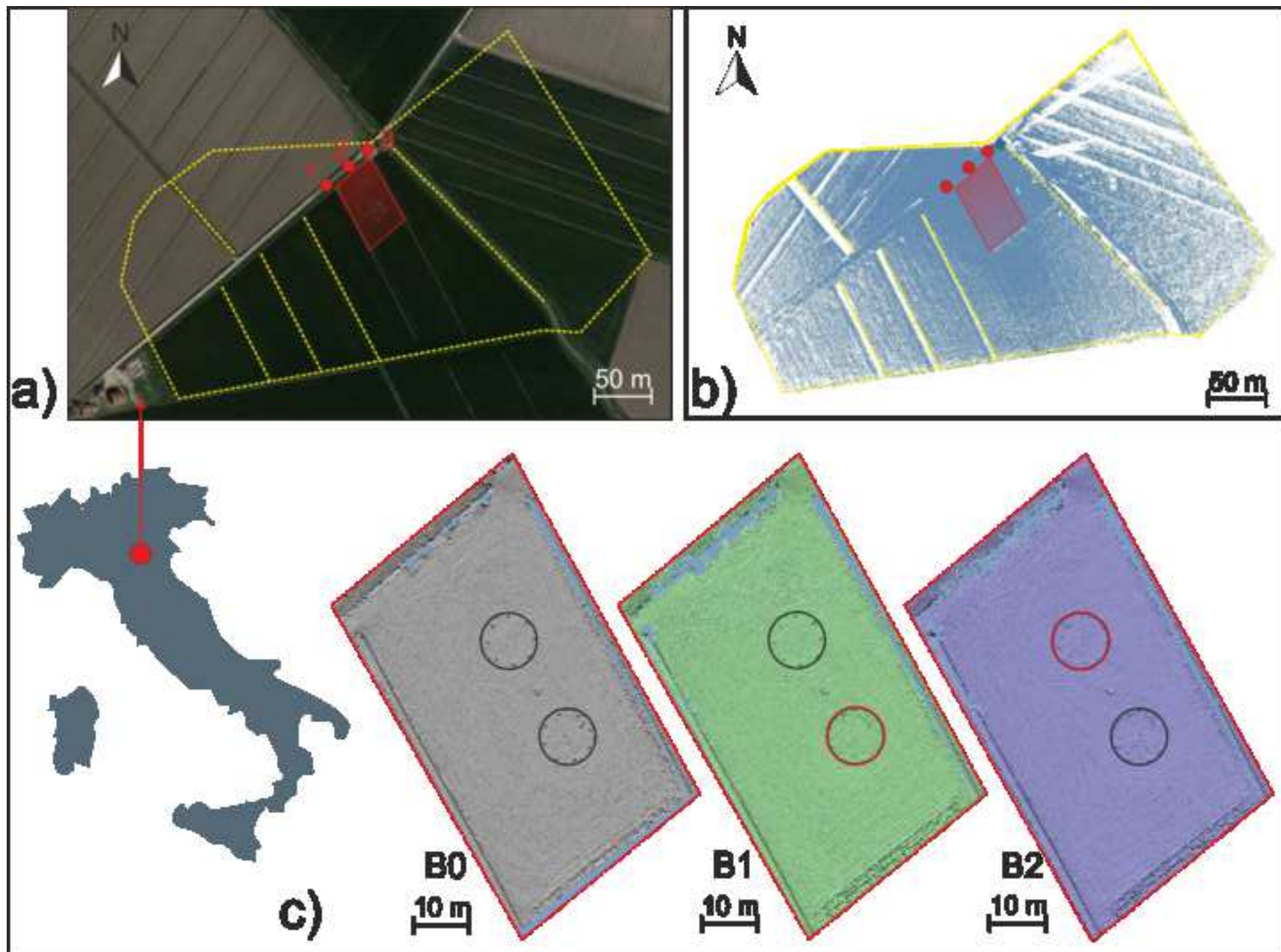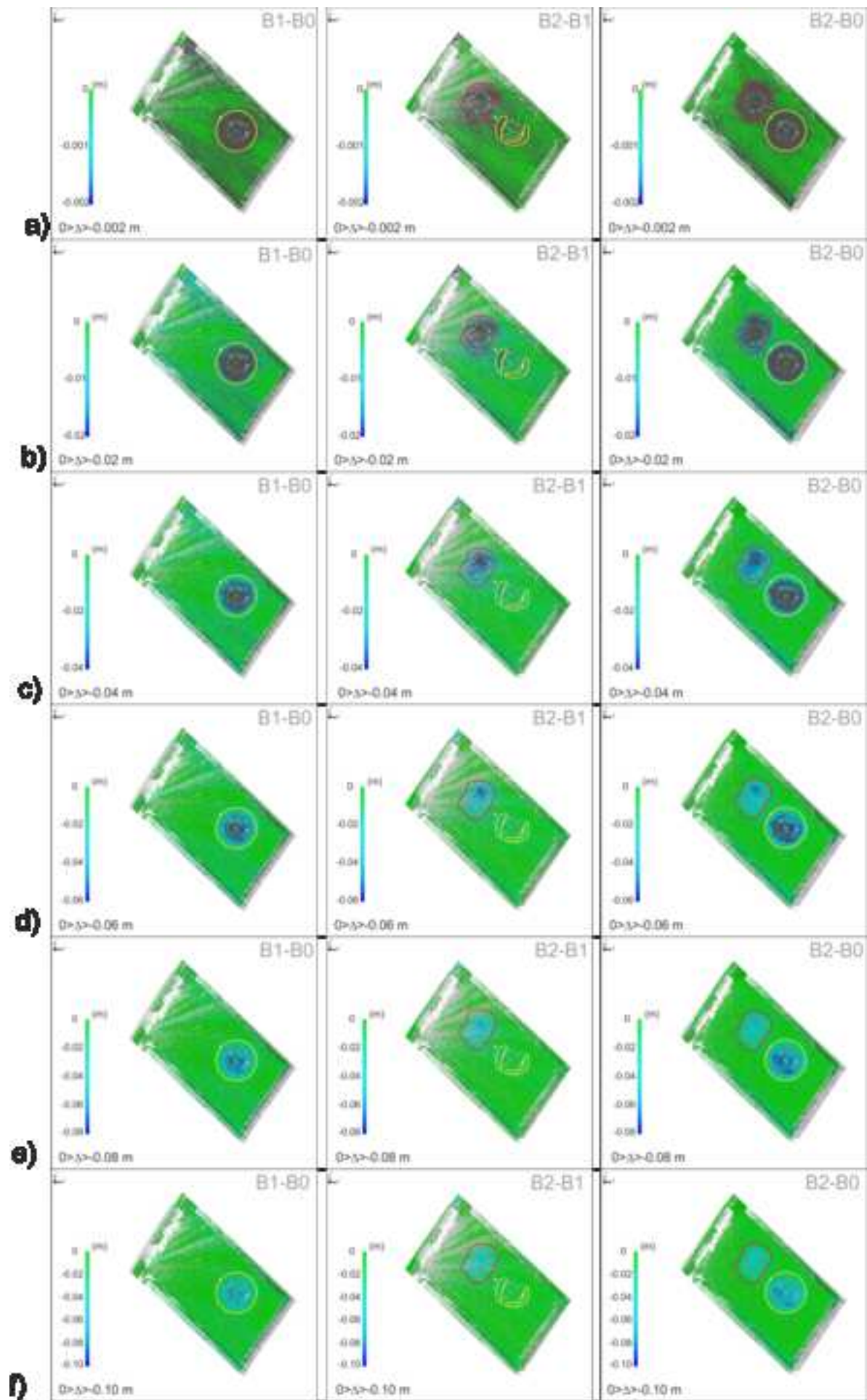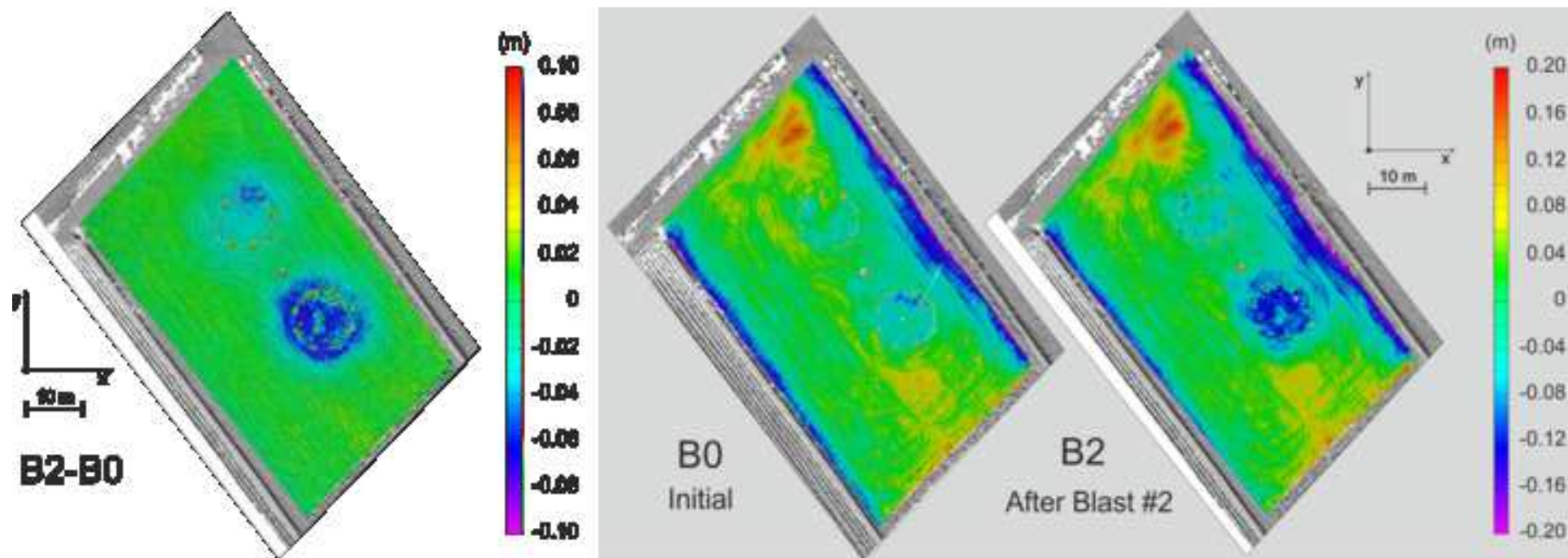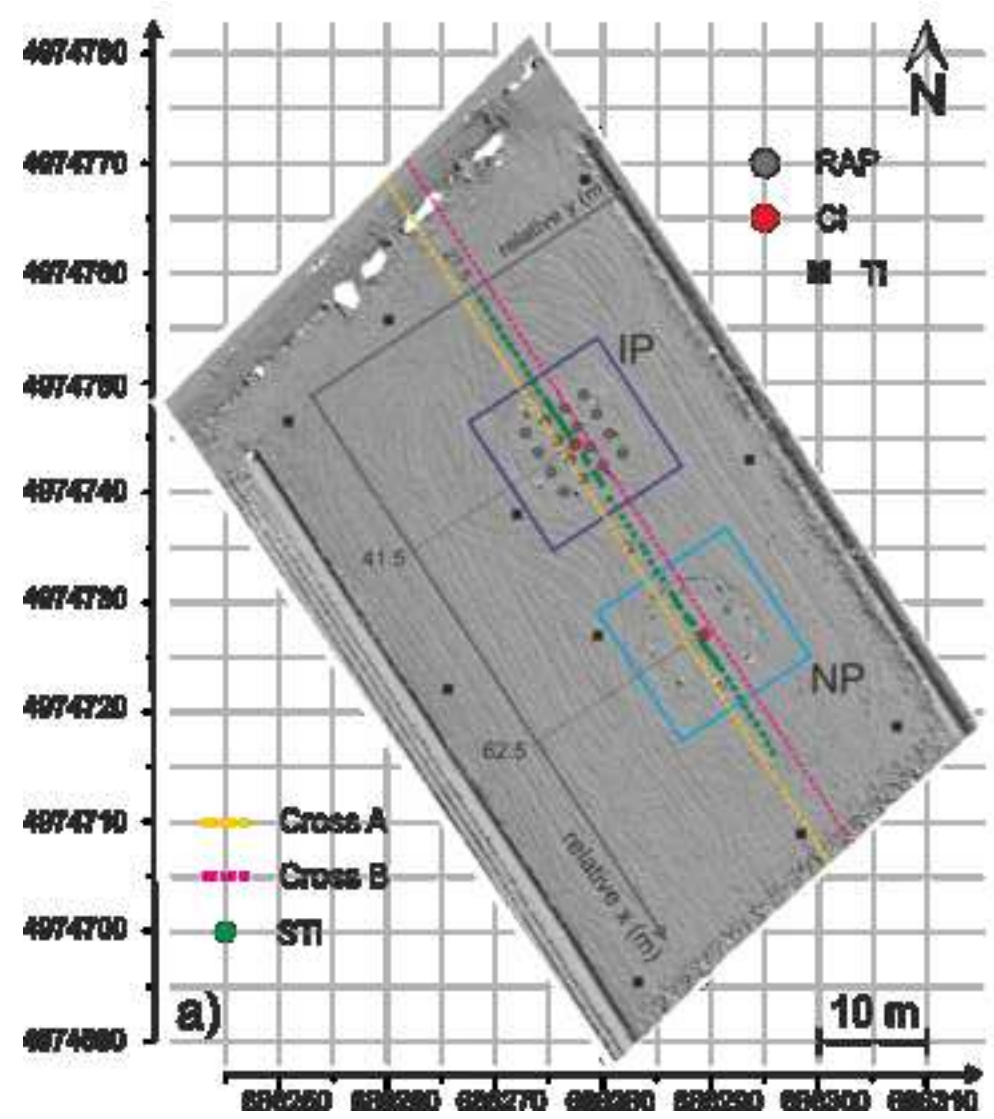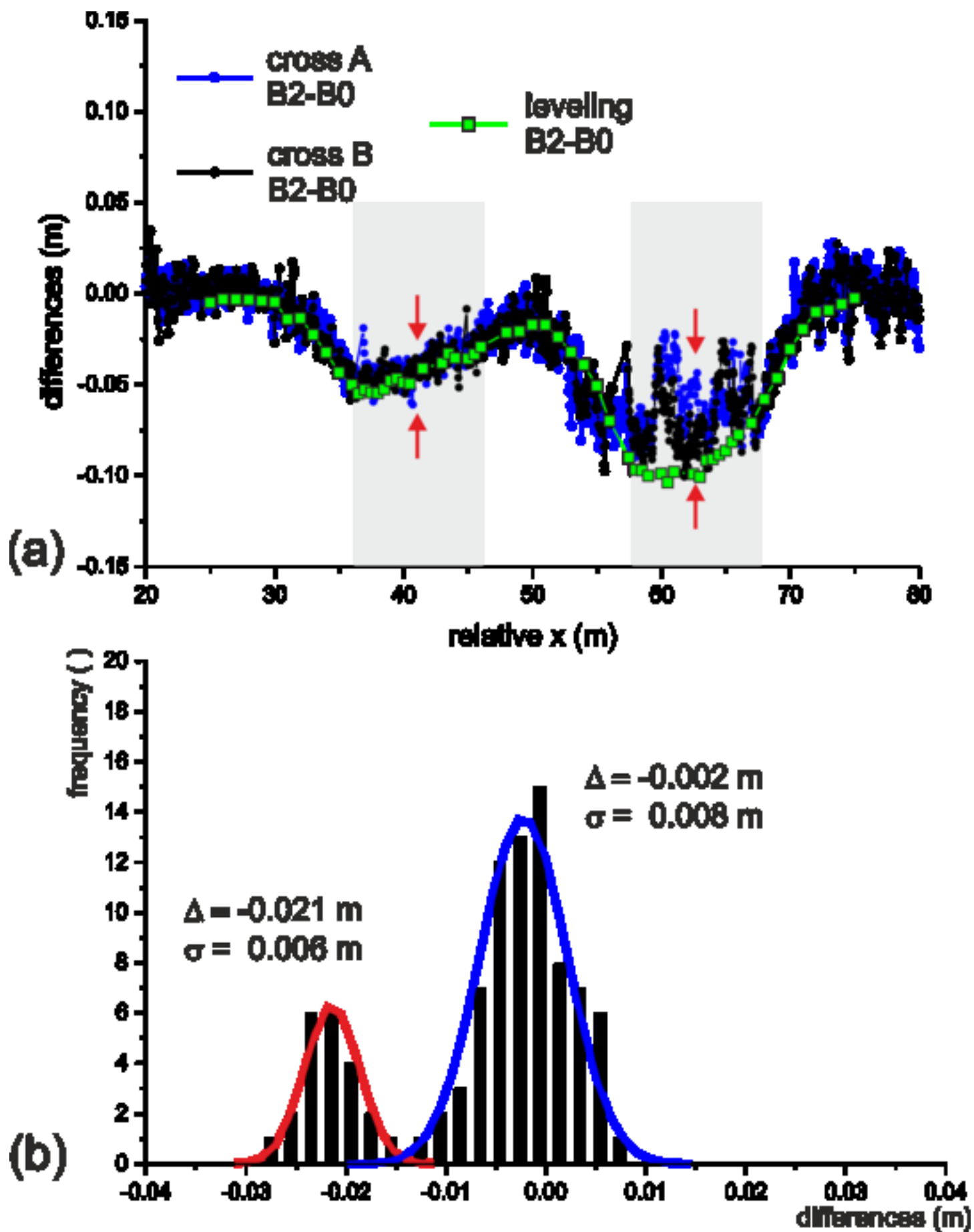
Figure 10

Figure 11

Figure captions

Figure 1. Basic geological/geotechnical information about Bondeno area: a) localization; b) schematic soils map of Emilia-Romagna, where plain and Apennine Mountains of different elevations are shows; c) soil stratigraphy, where the groundwater table depths in February 2018 (GWT1) and April 2018 (GWT2) are also shown, and CPT results in terms of total cone resistance (q_t) before and after RAP; d) map of depth to groundwater table.

Figure 2. A qualitative description of the experimental field from aerial images taken by a stationary drone before blasting. The two blast areas (IP and NP) are highlighted, together with the main topographical details such as the levelling line (dotted line) and the targets used to materialize the GCPs for georeferencing purposes.

Figure 3. TLS survey: a) aerial image of the area on which the TLS point cloud boundary (i.e. the ROI) is superimposed and where the TLS viewpoints are shown (points 1, 2 and 3); b) the complete point cloud obtained from the first survey(before the experiment); c) the three TLS point clouds of the ROI, where B0, B1 and B2 means the three experiment stages, i.e. pre-blast, post-blast1 and post-blast2.

Figure 4. Maps of differences in settlement (negative values), obtained from multitemporal TLS surveys, B1-B0, B2-B1, B2-B0 in the range: a) [-2 mm, 0]; b) [-20 mm, 0]; c) [-40 mm, 0]; d) [-60 mm, 0]; e) [-80 mm, 0]; f) [-100 mm, 0].

Figure 5. B2-B0 map of differences and B0 and B2 morphological maps representing the terrain surficial topography before and after the blast experiment.

Figure 6. SfM point clouds for B0, B1, B1b and B2 stages and zoom in NP and IP areas. The mean flight times are also shown (top right angle of each panel).

Figure 7. Comparison between the SfM models in the more suitable difference scale, i.e. the range [-8 cm, 0]. On the right column, a zoom-in of the NP area shows the "bowl" shaped settlement pattern around the blast center.

Figure 8. A comparison of ground settlement measurements obtained 30 minutes after the first blast in the NP, and the second blast in the IP along a line between the centers of the NP and IP. The combined settlement from B1 and B2 is shown with circles.

Figure 9. Cross-section generation: a) ROI, levelling points, targets and schematic features, where STi indicate the levelling stakes, Ti the targets for georeferencing, and Ci the blast area centers; b) B0, B1 and B2 from cross-section A (Cross A), where the arrows identify the centers of each blast panel; c) B0, B1 and B2 from cross-section B (Cross B).

Figure 10. Cross-sections generated from TLS data for B0, B1 and B2 stages: a) A cross-section, IP panel; b) B cross-section, IP panel; c) A cross-section, NP panel; d) B cross-section, NP panel. Arrows indicate the centers of each blast panel.

Figure 11. Height differences obtained from TLS data: a) along A cross-section; b) along B cross-section. The centers of NP and IP areas are indicated by the dashed lines.

Figure 12. a) Cumulative lowering, i.e. related to B2-B0, obtained from TLS along the cross-sections; b) histogram of differences between levelling and TLS elevations. Arrows identify the centers of each blast panel.